On the electrocatalytic symbiotic synergism between Pt, Ni and Al in plasma vapour deposited $Pt_xNi_yAl_z$ thin metal films for water electrolysis

Roelof J. Kriek[1]*, Liesel A. van Heerden[1], Anzel Falch[1], Malcolm I. Gillespie[2], Alaa Y. Faid[3], Frode Seland[3]

[1]Electrochemistry for Energy & Environment Group, Research Focus Area: Chemical Resource Beneficiation (CRB), North-West University, Private Bag X6001, Potchefstroom 2520, South Africa

[2]Demcotech Engineering, P.O. Box 9624, Edenglen, Johannesburg, 1645, South Africa

[3]Department of Materials Science and Engineering, Faculty of Natural Sciences, Norwegian University of Science and Technology, NO-7491 Trondheim, Norway

Abstract

This work highlights the fact that the activity of an already active metal/surface, i.e. Ni, can be increased even further by combining it with metals/surfaces that exhibit low activity, i.e. Pt and Al, when used on their own. Combinatorial screening was conducted on plasma vapour deposited $Pt_xNi_yAl_z$ thin-film ratios for the oxygen evolution reaction in alkaline medium. All co-deposited thin films were simultaneously evaluated employing a multichannel potentiostat with $Pt_9Ni_{56}Al_{35}$ exhibiting the highest current at 1.39 V (SHE). Subsequent deposition on a glassy carbon insert followed by electrochemical characterization revealed that $Pt_9Ni_{56}Al_{35}$ performed better than its constituent components in that it exhibited an overpotential of 487 mV at 10 mA.cm^{-2} compared to 590 mV, 941 mV, and 1379 mV for the overpotentials of vapour deposited Ni, Pt and Al respectively. Subsequent evaluation of co-deposited $Pt_9Ni_{56}Al_{35}$, as an electrocatalyst on a nickel woven mesh anode inside a membraneless divergent electrode-flow-through (DEFT^{TM}) alkaline electrolyser, resulted in a current density

of 1198 mA.cm^{-2} at a cell potential of 2 VDC. This represents the highest current density to date for a membraneless alkaline electrolyser.

***Corresponding author**: R.J. Kriek (cobus.kriek@nwu.ac.za)

Introduction

In the inaugural volume of Nature Energy the editor writes, "It's clear that dealing with climate change calls for deep (and likely, total) decarbonization of our energy system" [1]. To attain this 'holy grail', i.e. a renewable decarbonized energy system, will require of us to, not only turn our backs to the *status quo*, but to pursue disruptive technologies. This means that we will have to do things drastically different. For example, if we are to pursue a hydrogen economy with electrolysis being one of the enabling drivers, then we need to think differently about electrolysis. Is the current *status quo* of practicing electrolysis going to lead us down the path of attaining this energy 'holy grail'? In all likelihood the answer would be a resounding no, unless we start to think out of the box. This relates to both the electrolyser technology employed and the associated electrocatalyst for the oxygen evolution reaction (OER).

Electrolysis, for the production of hydrogen from water, can be divided into three categories at present, i.e. proton exchange membrane electrolysis (PEME), alkaline electrolysis, and solid oxide electrolysis. All three technologies make use of a membrane, or dense electrolyte, to separate the anode from the cathode so as to prevent the produced hydrogen and oxygen gases from mixing. In this sense membrane-based technologies can certainly be deemed as being the

status quo for current electrolysis technologies. If, however, one was to (i) develop an electrolyser that did not make use of a membrane, so as to simplify the design, and the ease of maintenance, and (ii) coat the electrodes with an extremely thin and durable electrocatalytic layer so as to substantially reduce the metal content of the electrocatalyst, would this go down as being disruptive? We believe so, if these changes/improvements were to translate into a more cost effective and efficient electrolyser system.

What would such a membraneless electrolyser look like and how would it operate? In 2015 Hashemi and co-workers [2] reported on their membraneless electrolyser that separates the produced hydrogen and oxygen gases based on what is termed the Segré-Silberberg effect. This relies on the produced gases co-existing next to each other while being kept apart by means of a parabola shaped laminar velocity profile, creating inertial lift forces that results in the migration of bubbles close to each respective electrode surface. The authors rightly point out that this principle of product gas separation is controlled by "the delicate balance between fluid mechanic forces in the device" [2], and as yet has to be proven to be able to keep gases apart in an upscaled facility, as this device has only been proven to operate at the miniature scale (comparable in size to a one Swiss Franc coin) at an electrolytic (1 M sulfuric acid) flow-rate of 14 ml.h^{-1} producing 300 mA.cm^{-2} at 2.6 V. In the same year we reported on a membraneless divergent electrode-flow-through (DEFT^{TM}) alkaline electrolyser (see Figure 1) that does not rely on the co-existence of the product gases as the produced hydrogen and oxygen are divergently flowing away from each other, in opposing directions, through porous electrodes [3]. Employing pure nickel mesh electrodes of 30 mm diameter, a current density of 326 mA.cm^{-2} was achieved at 2 V at an electrolytic flow-rate of 191 L.h^{-1}, which constitutes a substantial increase in scale. The current density, however, was increased to 474 mA.cm^{-2} at 2 V, at the same electrolytic flow-rate, by employing RuO$_2$/IrO$_2$/TiO$_2$ on the anode, in the ratio 35:10:55

and with a loading ranging between 35 and 65 g.m^{-2}, and Pt on the cathode [3]. RuO$_2$/IrO$_2$/TiO$_2$ is a common combinatorial rutile type anodic catalyst employed in the Chlor Alkali industry and is known for its effectiveness as an electrocatalyst for the OER [4,5]. IrO$_x$ on its own has also been used as control thin films for the evaluation of different metal oxide thin film electrocatalysts [6].
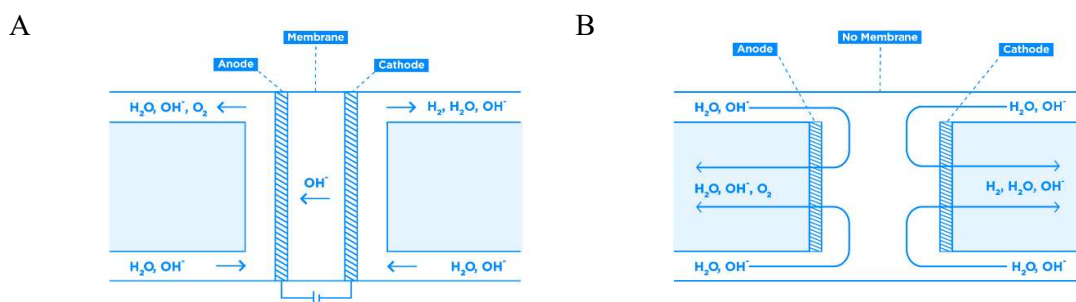
Figure 1   General operating principle of (a) an electrolyser that includes a membrane, and (b) the DEFT^{TM} membraneless electrolyser [3]

Although the OER activity of IrO$_2$ and RuO$_2$, in both acid and alkaline medium, are to date among the highest known [7], nickel and nickel-based materials are, however, widely regarded as preferred electrocatalysts for the OER in alkaline medium [8-16]. Raney nickel, a nickel aluminium alloy, has proven to be a very good and stable electrocatalyst [8,17], with activity and stability of the electrocatalyst both being crucial to the cost-effectiveness of the electrolysis process [18]. To that regard Kjartansdóttir *et al.* [10] prepared electrodes for a commercial membrane-based bipolar electrolyser stack by depositing aluminium onto a nickel substrate through plasma vapour deposition (PVD). Subsequent heat treatment facilitated alloy formation and was followed by selective aluminium leaching to produce a porous nickel layer. Their PVD Ni/Al electrodes exhibited a substantially lower overpotential compared to solid

nickel electrodes. This is in line with the reported synergistic interaction that exists between redox-active metal ions, in this instance Ni, and Lewis-acidic cations, in this instance Al [19].

Thin electrocatalytic films are attractive in that they, compared to thick electrocatalyst layers, reduce the distance that electrons have to travel to reach the current collector/substrate. The overpotential is therefore reduced and kept to a minimum as a result of the associated conductivity of the thin film electrocatalyst [20]. To further increase the OER current density, and to reduce the negative impact on nickel during electrolysis, we report here on our investigation into plasma vapour deposited (PVD) thin films of $Pt_xNi_yAl_z$ and on the evaluation of the preferred combination in the above-mentioned membraneless DEFT[TM] alkaline electrolyser [3].

Experimental

Through photolithography and plasma vapour deposition (PVD) an electronic circuit (Figure 2a), consisting of a layer of titanium (~10 nm) covered by a layer of gold (~100 nm), was produced on a 100 mm diameter silica wafer (Si + 200 nm SiO_2, Microchemicals GmbH). The circuit consisted of 64 working electrode pads, in a concentric arrangement, with each linked to a contact pad on the perimeter. All sputtering targets (99.99% Pt, 99.99% Ni and 99.999% Al) were sourced from ACI Alloys, USA. The plasma vapour deposition apparatus was custom built and supplied by PVD Products (Boston, USA). By means of process logic control, subsequent to calibration of the sputtering rate of each metal, different ratios of $Pt_xNi_yAl_z$ thin films (20 nm in thickness) were deposited through an aperture on each of the working electrode pads (Figure 2b). The wafer sat on a movable table, in the x- and y-directions, below the aperture. Electrochemical screening of the sputtered $Pt_xNi_yAl_z$ ratios was conducted in an in-

house custom-built electrochemical cell that consisted of a water-jacketed and Halar-coated (an ethylene chlorotrifluoroethylene (ECTFE) co-polymer) glass vessel for temperature control (employing a Julabo F12-ED refrigerated circulator). The cell housed a platinum coated perforated titanium disk as a counter electrode, a saturated calomel electrode (SCE, Radiometer) as the reference electrode (Figure 2c), with the 64 3 mm x 3 mm pads acting as working electrodes. The electrochemical cell was connected to a 64-channel potentiostat (MSTAT, Arbin Instruments). Linear polarisation scans were conducted at a scan rate of 20 $mV.s^{-1}$ in N_2 saturated 0.1 M KOH (Merck, uniVAR) at 25 °C.

Electrochemical kinetics were conducted employing a regular three-electrode RDE (rotating disk electrode) setup consisting of a working electrode rotator and a Pt counter electrode (both from Pine Instruments), as well as a SCE (Radiometer) as reference. Glassy carbon rods (SIGRADUR® G, 5 mm diameter) were obtained from HTW Germany, cut into 4 mm sections, and polished to a mirror finish on one end. These were employed as working electrode disk inserts onto which a specific $Pt_xNi_yAl_z$ ratio, identified through combinatorial screening, was deposited through magnetron sputtering. Milli-Q water (18 $\Omega.cm^{-1}$) was used to prepare all solutions and all electrolyte solutions consisted of 0.1 M KOH (Merck, uniVAR). Linear polarisation scans were conducted at 1600 rpm and a scan rate of 10 $mV.s^{-1}$ in N_2 saturated 0.1M KOH (Merck, uniVAR) at 25 °C. These scans were corrected for iR_u drop, employing BioLogic's ZIR technique, and all potentials were related to the reversible hydrogen electrode (RHE).
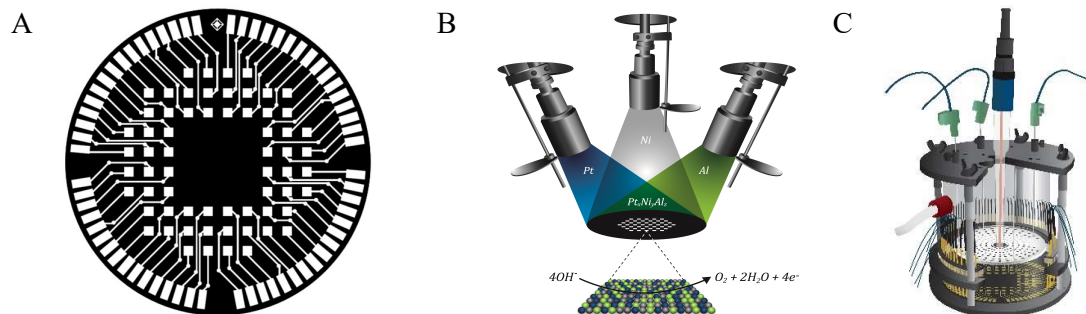
Figure 2 (a) Electronic circuit employed for the rapid screening of different electrocatalyst ratios deposited onto discrete working electrode pads (reprint permission granted) [21], (b) co-deposition of different $Pt_xNi_yAl_z$ ratios through magnetron sputtering, and (c) combinatorial screening cell (reprint permission granted) [22] for the simultaneous electrochemical screening of the deposited $Pt_xNi_yAl_z$ electrocatalysts

An investigation into the surface electronic states and composition of the best performing vapour-deposited electrocatalysts (deposited onto glassy carbon) were carried out employing X-ray photoelectron spectroscopy (XPS). XPS spectra were collected employing an Axis Ultra DLD instrument (Kratos Analytical, Manchester, UK) equipped with a monochromatic Al X-ray source (hv = 1486.6 eV). The glassy carbon disk inserts, onto which the thin films were deposited, were cut to a 2 mm height to fit into the XPS chamber. The chamber was pumped down to 10^{-10} Pa prior to analysis, and high-resolution spectra (Pt4f, Ni3p, Al2p, Al2s) were collected, with charge neutralisation having been applied during analysis.

Similar to XPS, grazing incidence angle x-ray diffraction (XRD) were conducted of the best performing vapour-deposited electrocatalysts (deposited onto glassy carbon) employing a Bruker D8 A25 DaVinci X-ray Diffractometer with Cu-K_α radiation and a LynxEye™ SuperSpeed Detector. The Göbel mirror was used to obtain a parallel beam, with the incident

grazing angle fixed at 2.5 °, while the scanning detector angle typically ranged between 35 and 90 degrees (2θ). All samples were measured employing the same scan conditions.

The best performing $Pt_xNi_yAl_z$ ratio, obtained from both wafer screening and RDE analysis, was sputtered onto a pure nickel mesh as the anode, and used in conjunction with a Pt-plated (electrochemical) nickel mesh as the cathode (35 – 65 g.m^{-2} Pt, NMT Electrodes Pty Ltd), for testing in a membraneless DEFT^{TM} alkaline electrolyser [3] (Figure 3). The electrolyser was operated at 70 °C, 30 wt% KOH as the electrolyte, an electrolytic flow-rate of 191 L.h^{-1}, and normal ambient pressure with a pressure drop of 1 – 2 kPa across the mesh electrodes.
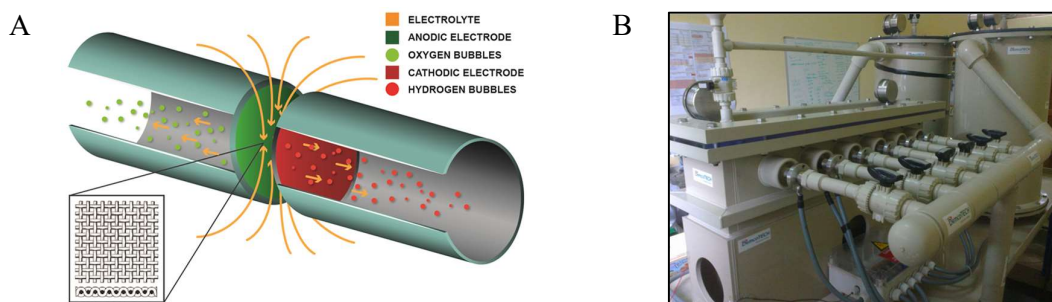
Figure 3   (a) Schematic diagram of the membraneless divergent electrode-flow-through (DEFT^{TM}) principle, and (b) the membraneless DEFT^{TM} pilot facility (reprint permission granted) [3]

Results & Discussion

Catalyst Combinatorial Screening

From the linear polarisation (LP) scans (Figure 4a), for the stationary vapour deposited $Pt_xNi_yAl_z$ ratios on the electronic circuit (Figure 2a) inside the combinatorial electrochemical cell (Figure 2c), it is clear that a wide range of current densities at specific overpotentials exist. Constructing a ternary diagram of the current for each ratio at 1.39 V (SHE), i.e. 2.15 V (RHE)

or 1.19 V (Hg/HgO), which is the highest potential where oxygen bubble formation does not affect the LP scan, one can observe that an area of high activity exists with Pt, Ni and Al ranging from 3 – 25 %, 50 – 65 %, and 20 – 55 % respectively, which translates into a metal content in descending order of Ni > Al > Pt (Figure 4b). It is furthermore clear, from this diagram (Figure 4b), that pure Pt and pure Al exhibit very low currents compared to that of pure Ni and the $Pt_xNi_yAl_z$ ratios. The eight ratios that exhibited the highest currents on the wafer are, in descending order, $Pt_9Ni_{56}Al_{35} > Pt_{12}Ni_{51}Al_{37} > Ni_{45}Al_{55} > Pt_{18}Ni_{43}Al_{39} > Pt_{20}Ni_{80} > Pt_3Ni_{62}Al_{35} > Ni_{33}Al_{67} > Pt_{16}Ni_{31}Al_{53}$.
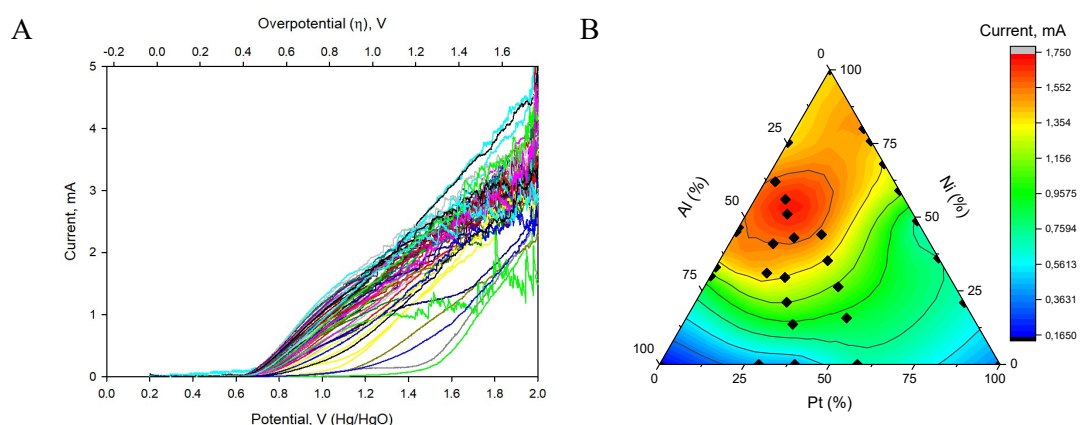
Figure 4   (a) Linear polarization scans of the different $Pt_xNi_yAl_z$ ratios on the wafer within the combinatorial electrochemical screening cell at 20 mV.s^{-1} in 0.1 M KOH, and (b) ternary diagram, based on the wafer data, showing the area of high activity for the $Pt_xNi_yAl_z$ ratios

The above-mentioned eight ratios, together with pure Pt, Ni, and Al, were subsequently sputtered onto glassy carbon electrode inserts and subjected to linear polarisation scans at 1600 rpm (Figure 5a). What is immediately evident is the fact that the ternary $Pt_xNi_yAl_z$ ratios all exhibit higher current densities than the individual metals. For the pure metals it is quite clear that Ni outperforms Pt by some margin, with regard to both current density and onset potential, with Al performing even worse than pure glassy carbon (GC). All but one of the ratios sputtered

perform well up to high overpotentials, with only $Ni_{33}Al_{67}$ passivating and reaching a limiting current at around 1.2 V overpotential. An alloy containing a greater amount of aluminium in comparison to nickel, i.e. $NiAl_3$ and Ni_2Al_3, are described to be highly leachable phases of Ni/Al and consequently explains the passivation of the $Ni_{33}Al_{67}$ alloy [10].

A bar graph of the overpotential (at 10 mA.cm^{-2}) for each sputtered thin film ratio, as well as for the individual metals and glassy carbon, reveal the following ascending order: $Pt_{16}Ni_{31}Al_{53}$ > $Pt_3Ni_{62}Al_{35}$ > $Pt_9Ni_{56}Al_{35}$ > $Pt_{20}Ni_{80}$ > $Pt_{12}Ni_{51}Al_{37}$ > $Ni_{45}Al_{55}$ > $Pt_{18}Ni_{43}Al_{39}$ > Ni > $Ni_{33}Al_{67}$ > Pt > Al (Figure 5b). Pure Al metal exhibits by far the greatest overpotential followed by glassy carbon (GC) and Pt, with the overpotentials for Ni, Pt and Al having been 590 mV, 941 mV, and 1379 mV respectively. What is quite intriguing is the fact that by co-depositing Ni with two poorer performing metals, i.e. Pt and Al, the overpotential for the oxygen evolution reaction in alkaline medium (0.1 M KOH) drops quite significantly to 459 mV for $Pt_{16}Ni_{31}Al_{53}$, 475 mV for $Pt_3Ni_{62}Al_{35}$, and 487 mV for $Pt_9Ni_{56}Al_{35}$, which is an improvement on that of pure Ni (590 mV) by more than 100 mV at 10 mA.cm^{-2}.

In addition to comparing the activity of the different ratios by means of (i) the current densities obtained on the wafer, and (ii) the overpotentials required to achieve a current density of 10 mA.cm^{-2} for the ratios sputtered onto glassy carbon inserts (employed in a RDE setup), the activity was furthermore interrogated by (iii) considering the Tafel slopes for the different electrocatalysts (employed in the RDE setup). From Table 1 it is evident that the ternary combinations, that include all three metals, i.e. Pt, Ni and Al, outperform the binary combinations (Ni and Al) followed by the single metals that exhibited highest Tafel slopes at increasingly higher overpotential regions. The Tafel slopes exhibited the following ascending

order: $Pt_3Ni_{62}Al_{35}$ > $Pt_{16}Ni_{31}Al_{53}$ > $Pt_{20}Ni_{80}$ > $Pt_{18}Ni_{43}Al_{39}$ > $Pt_9Ni_{56}Al_{35}$ > $Pt_{12}Ni_{51}Al_{37}$ > $Ni_{45}Al_{55}$ > $Ni_{33}Al_{67}$ > Ni > Pt > Al. Again, it is clear that combining Ni, which exhibited a Tafel slope of 127 mV.dec^{-1}, with Pt and Al, which exhibited Tafel slopes of around 200 mV.dec^{-1} and 700 mV.dec^{-1} respectively, ternary combinations are obtained that exhibit Tafel slopes less than 60 mV.dec^{-1}. It is, however, not clear what the role of each individual metal is, but it does seem clear that (a) $Pt_xNi_yAl_z$ surfaces, and (b) Pt being present in lesser quantities as part of $Pt_xNi_yAl_z$, are crucial in rendering a surface that is more amenable for attaining high activity for the OER.
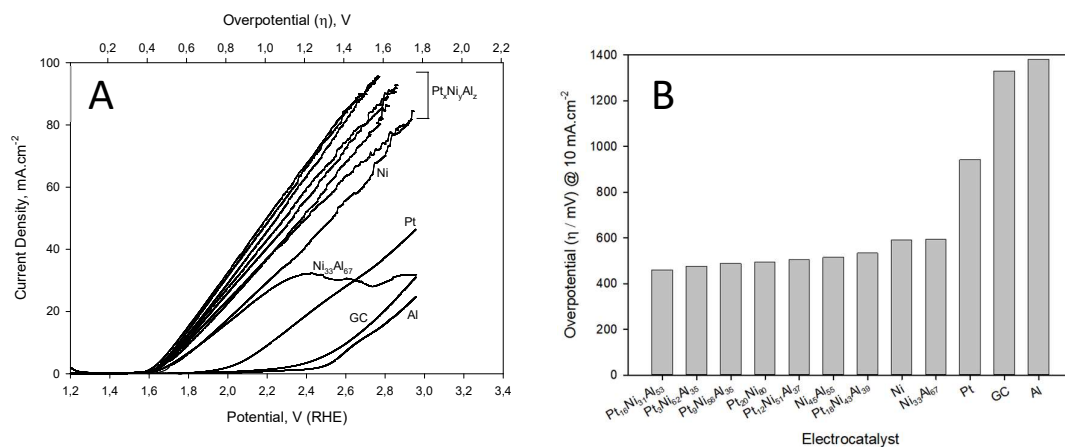
Figure 5　(a) Linear polarisation scans, in 0.1 M KOH at 1600 rpm and 25 °C, highlighting the fact that pure Pt, Ni and Al all exhibit lower electrocatalytic activity compared to certain $Pt_xNi_yAl_z$ ratios, and (b) overpotentials at 10 mA.cm^{-2} and 1600 rpm for the different $Pt_xNi_yAl_z$ electrocatalyst ratios (vapour deposited onto glassy carbon disk inserts)

Table 1 Tafel slopes for different Tafel regions for the different electrocatalysts

| Electrocatalyst | Tafel slopes / mV.dec^{-1} (Tafel region / mV) | | | |
	1	2	3	4
Pt$_{18}$Ni$_{43}$Al$_{39}$	50.1 (425 – 460)			
Pt$_{16}$Ni$_{31}$Al$_{53}$	56.3 (390 – 415)	47.0 (415 – 428)	41.6 (428 – 435)	
Pt$_{12}$Ni$_{51}$Al$_{37}$	53.9 (425 – 467)	66.2 (467 – 482)	82.8 (482 – 495)	
Pt$_9$Ni$_{56}$Al$_{35}$	52.8 (415 – 435)	50.6 (435 – 473)		
Pt$_3$Ni$_{62}$Al$_{35}$	42.9 (415 – 440)	36.3 (440 – 448)	33.5 (448 – 454)	29.6 (454 – 462)
Pt$_{20}$Ni$_{80}$	47.9 (425 – 465)			
Ni$_{45}$Al$_{55}$	60.8 (427 – 452)	72.8 (452 – 477)		
Ni$_{33}$Al$_{67}$	96.3 (444 – 475)	116.6 (475 – 496)		
Ni	127.0 (435 – 530)			
Pt	213.8 (720 – 783)	196.3 (783 -842)		
Al	905.9 (1070 – 1165)	706.4 (1165 – 1182)	556.8 (1182 – 1200)	

Surface Composition

The XPS spectra of the five best performing Pt$_x$Ni$_y$Al$_z$ electrocatalyst ratios did not reveal the presence of any contaminants (Figure 6). The High-resolution Pt 4f spectra are shown in Figure 6a, with the peaks at 71.08 eV and 74.40 eV that can be deconvoluted into two double components. For sample Pt$_{100}$, the binding energies located at 71.01 eV and 74.30 eV can be attributed to Pt 4f$_{7/2}$ and Pt 4f$_{5/2}$ and are assigned to Pt^0 species. The binding energies located at 71.51 eV and 75.3 eV can be assigned to Pt 4f$_{7/2}$ and Pt 4f$_{5/2}$ of Pt^{2+} species [23]. This is mainly due to most of the platinum atoms on the surface that can be easily oxidised in air before testing [24]. In the Pt alloys, the Pt 4f$_{7/2}$ peak at 71.08 shifted to higher energies with 0.1, 0.13, 0.18, 0.21 eV while the 4f$_{5/2}$ peak at 74.40 eV shifted to higher energy with 0.11, 0.14, 0.16, 0.18 eV for Pt$_{20}$Ni$_{80}$, Pt$_9$Ni$_{56}$Al$_{35}$, Pt$_{16}$Ni$_{31}$Al$_{53}$, and Pt$_3$Ni$_{62}$Al$_{35}$ respectively, which may be due to electronic interactions between the atomic orbitals of Pt and other metals [25-27]. High-resolution

XPS spectra of Ni 2p is shown in Figure 6b. Ni 2p in the high-resolution XPS region are derived from multi-electron excitation. When considering the two satellites peaks, the peaks located at 852.72 eV and 869.88 eV can be indexed to Ni $2p_{3/2}$ and Ni $2p_{1/2}$ of metallic Ni^0, while the peaks at 855.97 and 873.69 eV can be indexed to Ni $2p_{3/2}$ and Ni $2p_{1/2}$ of Ni^{2+} species in the forms of NiO and/or $Ni(OH)_2$ due to Ni surface oxidation [23, 28]. The Ni 2p spectra exhibit a slight shift of 0.1 eV when alloying Ni with Pt and Al in $Pt_{20}Ni_{80}$, $Pt_9Ni_{56}Al_{35}$, $Pt_{16}Ni_{31}Al_{53}$, and $Pt_3Ni_{62}Al_{35}$ due to electronic interactions between the atomic orbitals of Pt and other metals [25-27]. High-resolution Al 2p XPS spectra of the samples are shown in Figure 6c. For the Al_{100} sample, the peaks located at 70.85 and 74.2 eV are attributed to the spin-orbit splitting of Al^0 2p metallic and Al^{3+} 2p oxide state respectively. Both Al^0 2p and Al^{3+} 2p peaks exhibit peak shifting to higher energy (eV) due to alloying. Al^0 2p has a peak shift of 0.35, 0.4, and 0.43 eV, while Al^{3+} 2p has a peak shift of 0.33, 0.38, and 0.42 eV for $Pt_9Ni_{56}Al_{35}$, $Pt_{16}Ni_{31}Al_{53}$, $Pt_3Ni_{62}Al_{35}$ respectively [29]. High-resolution Al 2s is shown in Figure 6d, with the peak at 118.15 eV binding energy being attributed to Al 2s. Al appears to be in the oxidized state as thin films were exposed to air, [21] with Al^{3+} that can in all likelihood be attributed to the presence of Al_2O_3. This, however, could not be confirmed by grazing incident X-ray diffraction due to carbon (glassy carbon) peak broadening (Figure 7).
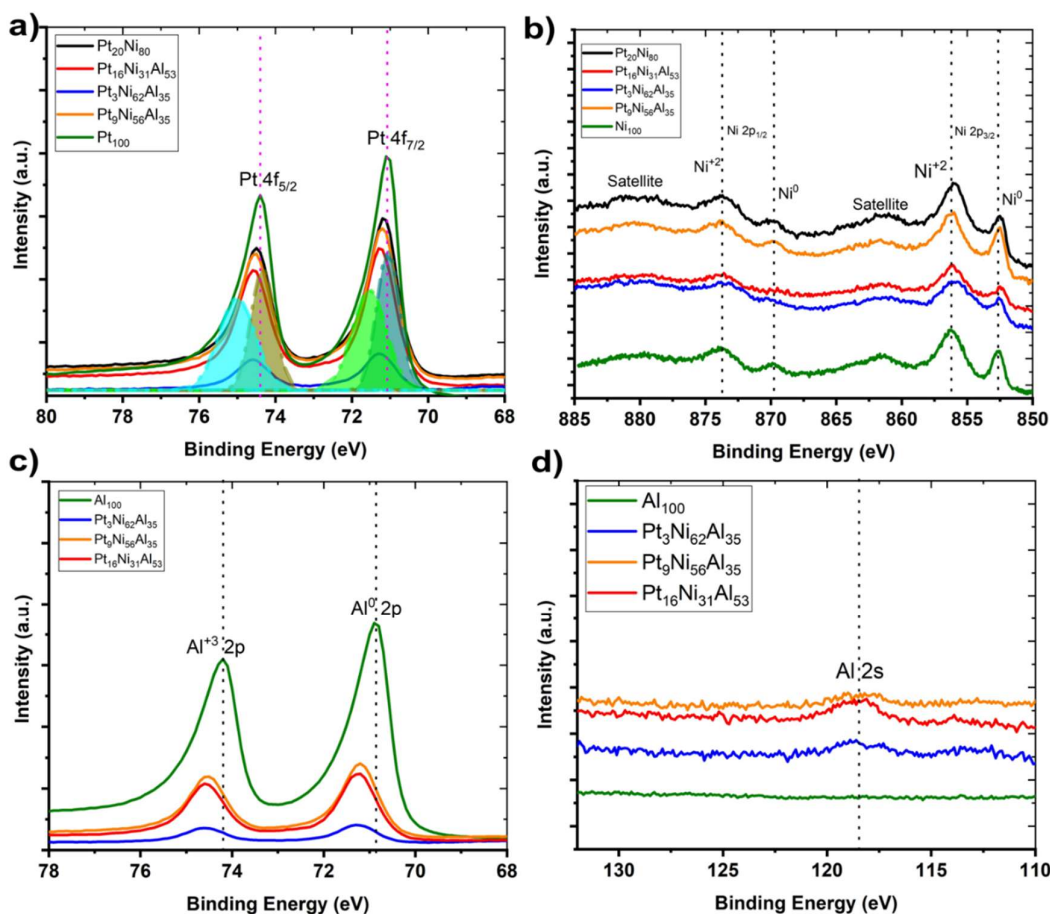
Figure 6 XPS spectra of the best performing $Pt_xNi_yAl_z$ electrocatalyst ratios showing (a) the Pt 4f spectra, (b) the Ni 2p spectra, (c) the Al 2p spectra, and (d) the Al 2s spectra.

Figure 7 shows the XRD patterns of the sputtered thin films using a grazing incidence angle of 2.5 °. Most of the XRD patterns display Bragg reflection that can be attributed to the underlying glassy carbon substrate as X-rays penetrate the thin sputtered layers to reach the GC substrate. Carbon is very transparent for X-rays, which results in peak broadening, [21] with carbon exhibiting two broad peaks at 43.3 ° and 78.8 °. It is worth pointing out that NiO with a face-centered cubic crystal structure has a characteristic peak at 43.2° [30] and Al_2O_3 has a characteristic peak at 43.4°, [31] which cannot be observed due to carbon peak broadening. The Pt thin film XRD pattern in Figure 7 shows reflections at 2θ-values of 39.74 °, 46.12 °, 67.44

°, and 81.07 °, which can be associated with the (111), (200), (220) planes of Pt face-centered cubic (Pt-FCC) crystalline structure [32-37]. Even though grazing incident x-ray diffraction was employed, due to the thin sputtered layers obtained, it is clear that (apart from platinum) no crystalline phases could be detected.
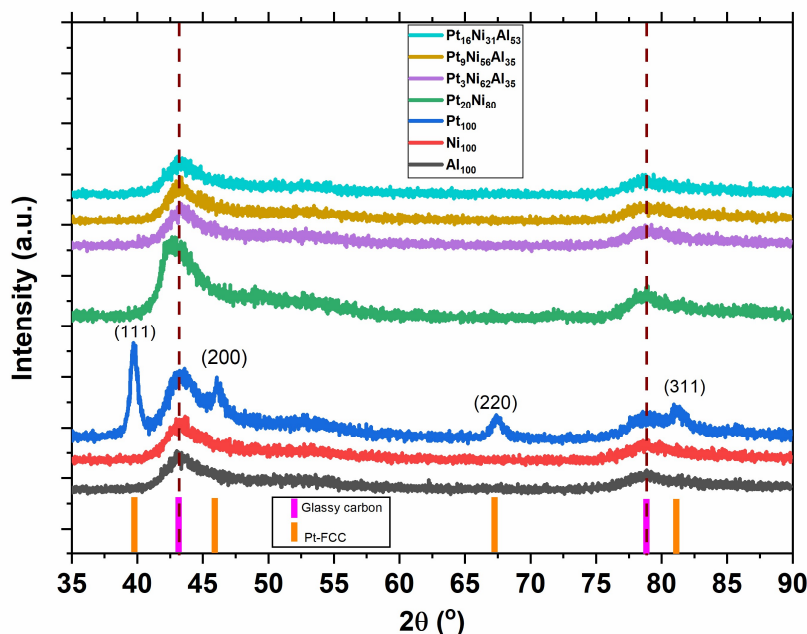
Figure 7 Grazing incident X-ray diffraction patterns of sputtered thin films of Pt, Ni, Al, and combinations thereof, with the vertical dotted lines showing peak position for all compositions.

Alkaline Electrolyser Performance

$Pt_9Ni_{56}Al_{35}$, performing well (on average) on the wafer and the RDE insert, was subsequently put to the test in a pilot DEFT™ membraneless alkaline electrolyser facility (Figure 3) [3], as these systems show a lot of promise and have been obtaining increasing attention as of late [38-40]. As already mentioned, a current density of 326 mA.cm^{-2} was achieved at 2 VDC at an electrolytic flow-rate of 191 L.h^{-1}, employing a pure nickel mesh anode and cathode. However, the current density increased to 474 mA.cm^{-2} at 2 VDC and the same electrolytic flow-rate by

employing a state-of-the-art $RuO_2/IrO_2/TiO_2$ on the mesh anode and Pt on the mesh cathode. In comparison, operating the DEFT^{TM} membraneless alkaline electrolyser (under the same conditions) with a PVD thin-film of $Pt_9Ni_{56}Al_{35}$ on the nickel mesh anode and Pt on the mesh cathode (at a 2.5 mm electrode gap), revealed a vastly superior performance in comparison to the pure nickel mesh electrodes (anode and cathode) as well as the $RuO_2/IrO_2/TiO_2$ anode and Pt cathode. At 1.75 VDC the $Pt_9Ni_{56}Al_{35}$ OER electrocatalyst yielded 477 mA.cm^{-2}, which represents a more than two-fold increase compared to the $RuO_2/IrO_2/TiO_2$ OER electrocatalyst. At 2 VDC the $Pt_9Ni_{56}Al_{35}$ electrocatalyst yielded an impressive 1199 mA.cm^{-2}, which is 153% greater than the $RuO_2/IrO_2/TiO_2$ OER electrocatalyst (Figure 8a). This high current density represents the highest obtained for a membraneless alkaline system, and has assisted to narrow the gap substantially between alkaline and PEM systems. For PEM systems, however, varying current densities are communicated. A current density of ~1036 mA.cm^{-2} has been reported at a cell voltage of 1.8 V for a PEM electrolyser operating at 80 °C and 1 bar with a 200 μm thick membrane [41]. Decreasing the membrane thickness to 150 μm, for the same electrolyser under the same conditions, the current density increases to ~1446 mA.cm^{-2}. This still represents a substantial advantage if the two technologies (PEM and membraneless alkaline water electrolysis) are compared purely on the basis of current density. It does, however, highlight the fact that the membrane has a negative effect on current density as thinner membranes result in increased ion conductivity, reduced resistance, reduced iR-drop, and ultimately increased current density. This serves to highlight the fact that getting rid of the membrane altogether only serves to benefit the technology, both from a performance point of view and a maintenance point of view, granted that small interelectrode distances with high electrolyte conductivity can be secured. Electrode gap and electrolyte flow rate were optimised in a previous work [3], and the impact is clearly illustrated in Figure 9a for the nickel mesh electrodes, where a higher flow rate and lower gap distance significantly improves the performance. In contrast, however, the

NOW study [42] conducted by the Fraunhofer Institute reports current densities for PEM systems ranging from 600 mA.cm^{-2} to 2000 mA.cm^{-2} at cell voltages of 1.8 V to 2.2 V respectively and temperatures ranging from 30 to 50 °C. The Fraunhofer Institute reports current densities for regular membrane-based alkaline water electrolysis to range between 200 and 400 mA.cm^{-2} at cell voltages of 1.8 V to 2.4 V respectively and temperatures ranging from 60 to 80 °C [42]. Their long-term forecast for alkaline water electrolysis (10 to 20 years post 2011) puts current density at < 800 mA.cm^{-2} between 1.7 and 2.2 V at temperatures ranging from 60 to 90 °C. This target has been surpassed by the DEFT^{TM} membraneless alkaline water electrolysis system employing a vapour deposited thin film of $Pt_9Ni_{56}Al_{35}$.

Ni-Fe based catalysts have become popular as OER electrocatalysts, however, they remain in the research and development phase due to their inability to remain stable for long durations of operation [43]. At an applied anodic current density of 10 mA.cm^{-2} in 0.1 M KOH solution, various Ni-Fe compositional combinations achieved overpotentials of between 462 – 532 mV, compared to IrO_2 that is described as the current state-of-the-art that achieved an overpotential of 350 mV at the same conditions [44]. In fact, it has been mentioned that IrO_x films are suitable controls for comparison to other electrocatalysts [6]. In their work, comparing different solution-cast metal oxide thin films as electrocatalysts for the oxygen evolution reaction alkaline medium, Trotochaud *et al*. [6] have shown that pure nickel oxide, in addition to nickel oxides doped with Fe and Co, outperform IrO_x substantially. From their work it is clear that, in comparison to the nickel-based oxides, IrO_x exhibits comparable overpotentials at lower current densities, which is typically the case for lab-scale setups. At greater current densities, however, which will be the case for commercial electrolysers, IrO_x exhibits much greater overpotentials that point to poorer efficiencies. It is evident that the $Pt_9Ni_{56}Al_{35}$ OER electrocatalyst demonstrates performance similar to that of the Ni-Fe combinations, however,

the $Pt_9Ni_{56}Al_{35}$ OER electrocatalyst has furthermore proven to be highly effective at enhancing the performance of a pilot DEFT™ membraneless alkaline electrolyser test facility. In addition, the PGM (platinum group metal) loading of the $Pt_9Ni_{56}Al_{35}$ thin film electrocatalyst is low (~ 4.2 x 10^{-6} g.cm^{-2} for the mesh electrode), which is beneficial as high PGM loadings are deemed unpractical due to their high cost contribution to the stack [43]. Durability studies, at present, are inconclusive as chronoamperometry investigations were unsuccessful in that the sputtered thin films (over time) delaminated from the glassy carbon support. Additional durability/lifetime studies on these $Pt_xNi_yAl_z$ electrocatalysts are, however, yet to be conducted.

Comparing the pros and cons of acidic PEM water electrolysis, regular alkaline water electrolysis, and improved alkaline water electrolysis (see Figure 8b), it is known that the main drawback of alkaline water electrolysers is that they suffer from low current densities, i.e. a low H_2 gas production rate relative to electrode size, compared to acidic PEM water electrolysers. Furthermore, the inherent environment of an acidic PEM electrolyser is more aggressive than that of an alkaline electrolyser, which makes the use of noble metal-based electrocatalysts, such as Pt and IrO_2, crucial in withstanding this aggressive environment. This results in (i) increased costs associated with PEM electrolysers, due to their high noble metal content, and (ii) lower efficiencies of alkaline electrolysers due to the lower H_2 gas production rates. In addition, a paper entitled "*The frontiers of energy*", also published as part of the inaugural issue of Nature Energy, makes the following two statements related to the membrane that form part of acidic PEM and alkaline electrolysers respectively, i.e. "Costs could be reduced by replacing the Nafion with cheaper alternatives that still provide the necessary proton conductivity, gas-blocking properties and stability under highly oxidative conditions", and "Membranes that are highly conductive towards selective transport of OH$^-$ ions and are stable at elevated temperatures would enable more compact, less expensive alkaline electrolysers" [45].

All of the above-mentioned 'issues' of (a) high noble metal content for acidic PEM electrolysers, (b) the low H_2 gas production rate of alkaline electrolysers, and (c) the associated limitations and problems with membranes, are alleviated by getting rid of the membrane altogether in employing the DEFT™ membraneless alkaline electrolyser coupled with a highly active anode electrocatalysts such as $Pt_9Ni_{56}Al_{35}$. This vastly improves the H_2 gas production rate of an alkaline electrolyser at a fraction of the Pt content of an acidic PEM electrolyser.
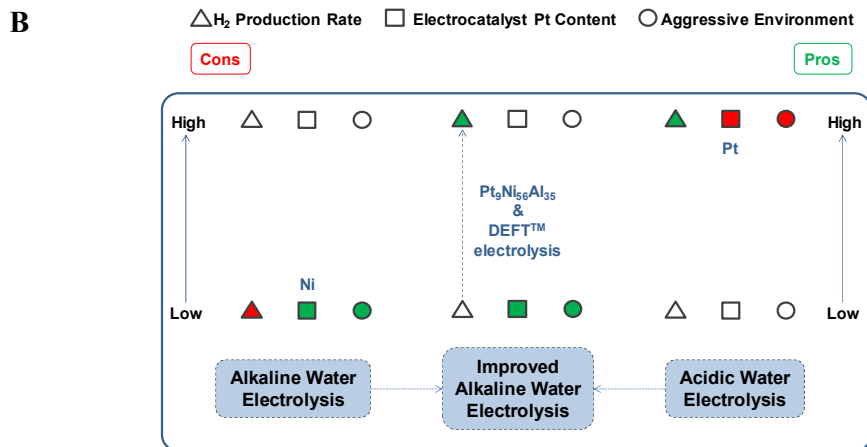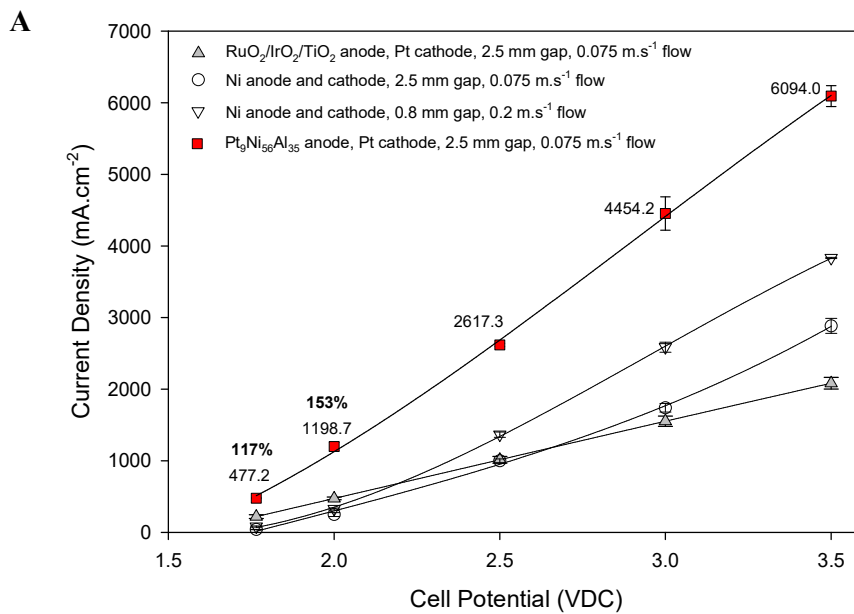
Figure 8   (a) Current densities obtained for the membraneless DEFT^{TM} pilot facility employing different anodic and cathodic electrocatalyst combinations at 70 °C and 30 wt% KOH, and (b) the comparison between regular alkaline and acidic water electrolysis on the one hand and improved alkaline water electrolysis on the other based on a $Pt_9Ni_{56}Al_{35}$ anode and the DEFT^{TM} membraneless principle

Conclusions

$Pt_xNi_yAl_z$ thin films, of different ratios, were co-deposited onto a silica wafer, through plasma vapour deposition, for screening in a combinatorial electrochemical cell for the OER in alkaline medium (0.1M KOH). Combining Ni with two inferior performing metals, i.e. Pt and Al, resulted in several x:y:z ratios that outperformed pure Ni by some margin (> 100 mV drop in overpotential at 10 mA.cm^{-2}). Of these $Pt_9Ni_{56}Al_{35}$ was observed to be (on average) the most active, which include both the static wafer and RDE investigations (overpotential values and Tafel slopes), exhibiting an overpotential of 487 mV at 10 mA.cm^{-2}. Application of $Pt_9Ni_{56}Al_{35}$ as a sputtered thin film electrocatalyst on the mesh anode of a membraneless DEFT^{TM} alkaline electrolyser, together with a Pt coated mesh cathode, resulted in a high current density (1198 mA.cm^{-2} at 2 VDC) that outperformed $RuO_2/IrO_2/TiO_2$ on the anode (474 mA.cm^{-2} at 2 VDC). This high current density, for an alkaline water electrolysis system, closes the gap substantially between PEM and alkaline systems. Although the overpotential at 10 mA.cm^{-2} is not the lowest reported, this work highlights the fact that metals (active and inactive) can be combined to produce a new surface that outperforms each distinct metal surface. This work furthermore points to the fact that there does not seem to be a clear link between electrocatalyst activities achieved on bench-top scale facilities, on the one hand, and pilot-scale facilities, on the other hand. This would certainly seem to be the case for a regular bench-top RDE facility and a pilot DEFT^{TM} alkaline electrolyser facility.

Acknowledgement

References

1. Editorial, A World in Transition, *Nat. Energy* **2016,** 1 (1), 1.

2. Hashemi, S. M. H.; Modestino, M. A.; Psaltis, D., A Membrane-less Electrolyzer for Hydrogen Production across the pH Scale, *Energy Environ. Sci.* **2015,** 8 (7), 2003-2009.

3. Gillespie, M. I.; van der Merwe, F.; Kriek, R. J., Performance Evaluation of a Membraneless Divergent Electrode-Flow-Through (DEFT) Alkaline Electrolyser based on Optimisation of Electrolytic Flow and Electrode Gap, *J. Power Sources* **2015,** 293, 228-235.

4. Rossmeisl, J.; Qu, Z.-W.; Zhu, H.; Kroes, G.-J.; Nørskov, J. K., Electrolysis of Water on Oxide Surfaces, *J. Electroanal. Chem.* **2007,** 607 (1-2), 83-89.

5. Miles, M.; Klaus, E.; Gunn, B.; Locker, J.; Serafin, W.; Srinivasan, S., The Oxygen Evolution Reaction on Platinum, Iridium, Ruthenium and their Alloys at 80 °C in Acid Solutions, *Electrochim. Acta* **1978,** 23 (6), 521-526.

6. Trotochaud, L.; Ranney, J. K.; Williams, K. N.; Boettcher, S. W., Solution-cast Metal Oxide Thin Film Electrocatalysts for Oxygen Evolution, *J. Am. Chem. Soc.* **2012,** 134 (41), 17253-17261.

7. Lee, Y.; Suntivich, J.; May, K. J.; Perry, E. E.; Shao-Horn, Y., Synthesis and Activities of Rutile IrO_2 and RuO_2 Nanoparticles for Oxygen Evolution in Acid and Alkaline Solutions, *J. Phys. Chem. Lett.* **2012,** 3 (3), 399-404.

8. Choquette, Y.; Menard, H.; Brossard, L., Electrocatalytic Performance of Composite-coated Electrodes for Alkaline Water Electrolysis, *Int. J. Hydrogen Energ.* **1990,** 15 (1), 21-26.

9. Li, X.; Walsh, F. C.; Pletcher, D., Nickel Based Electrocatalysts for Oxygen Evolution in High Current Density, Alkaline Water Electrolysers, *Phys. Chem. Chem. Phys.* **2011,** 13 (3), 1162-7.

10. Kjartansdottir, C. K.; Nielsen, L. P.; Møller, P., Development of Durable and Efficient Electrodes for Large-scale Alkaline Water Electrolysis, *Int. J. Hydrogen Energ.* **2013,** 38 (20), 8221-8231.

11. McCrory, C. C.; Jung, S.; Peters, J. C.; Jaramillo, T. F., Benchmarking Heterogeneous Electrocatalysts for the Oxygen Evolution Reaction, *J. Am. Chem. Soc.* **2013,** 135 (45), 16977-16987.

12. Kjartansdóttir, C.; Caspersen, M.; Egelund, S.; Møller, P., Electrochemical Investigation of Surface Area Effects on PVD Al-Ni as Electrocatalyst for Alkaline Water Electrolysis, *Electrochim. Acta* **2014,** 142, 324-335.

13. Seetharaman, S.; Balaji, R.; Ramya, K.; Dhathathreyan, K.; Velan, M., Electrochemical Behaviour of Nickel-based Electrodes for Oxygen Evolution Reaction in Alkaline Water Electrolysis, *Ionics* **2014,** 20 (5), 713-720.

14. Han, G.-Q.; Liu, Y.-R.; Hu, W.-H.; Dong, B.; Li, X.; Shang, X.; Chai, Y.-M.; Liu, Y.-Q.; Liu, C.-G., Three Dimensional Nickel Oxides/Nickel Structure by In Situ Electro-oxidation of Nickel Foam as Robust Electrocatalyst for Oxygen Evolution Reaction, *Appl. Surf. Sci.* **2015,** 359, 172-176.

15. Khan, S. B.; Khan, S. A.; Asiri, A. M., A Fascinating Combination of Co, Ni and Al Nanomaterial for Oxygen Evolution Reaction, *Appl. Surf. Sci.* **2016,** 370, 445-451.

16. Le Formal, F.; Guijarro, N.; Bourée, W. S.; Gopakumar, A.; Prévot, M. S.; Daubry, A.; Lombardo, L.; Sornay, C.; Voit, J.; Magrez, A., A Gibeon Meteorite Yields a High-performance Water Oxidation Electrocatalyst, *Energy Environ. Sci.* **2016,** 9 (11), 3448-3455.

17. Delgado, D.; Bizzotto, F.; Zana, A.; Arenz, M., Accelerated Durability Test for High-Surface-Area Oxyhydroxide Nickel Supported on Raney Nickel as Catalyst for the Alkaline Oxygen Evolution Reaction, *ChemPhysChem* **2019,** 20 (22), 3147-3153.

18. Li, G., Anderson, L., Chen, Y., Pan, M. & Chuang, P. Y. A. New insights into evaluating catalyst activity and stability for oxygen evolution reactions in alkaline media. *Sustain. Energy Fuels* **2018**, 2, 237-251.

19. Gerken, J. B.; Shaner, S. E.; Massé, R. C.; Porubsky, N. J.; Stahl, S. S., A Survey of Diverse Earth Abundant Oxygen Evolution Electrocatalysts Showing Enhanced Activity from Ni–Fe Oxides Containing a Third Metal, *Energy Environ. Sci.* **2014**, 7 (7), 2376-2382.

20. Trotochaud, L.; Boettcher, S. W., Precise Oxygen Evolution Catalysts: Status and Opportunities, *Scr. Mater.* **2014**, 74, 25-32.

21. Falch, A.; Badets, V.A.; Labrugère, C.; Kriek, R.J., Co-sputtered $Pt_xPd_yAl_z$ thin film electrocatalysts for the production of hydrogen via SO_2(aq) electro-oxidation, *Electrocatalysis*, 2016, 7, 376-390.

22. Falch, A.; Lates, V.; Kriek, R.J., Combinatorial Plasma Sputtering of Pt_xPd_y Thin Film Electrocatalysts for Aqueous SO2 Electro-oxidation, *Electrocatalysis* 2015, 6 (3), 322-330

23. Wang, Z.; Lu, C.; Kong, W.; Zhang, Y.; Li, J., Platinum nanoparticles supported on core–shell nickel–carbon as catalyst for methanol oxidation reaction, *J. Alloys Compd.*, **2017**, 690, 95-100.

24. Zhu, L.; Zheng, T.; Yu, C.; Zheng, J.; Tang, Z.; Zhang, N.; Shu, Q.; Chen, B.H., Platinum-nickel alloy nanoparticles supported on carbon for 3-pentanone hydrogenation, *Appl. Surf. Sci.*, **2017**, 409, 29-34.

25. Zheng, J.; Zhao, Y.; Xi, H.; Li, C., Seawater splitting for hydrogen evolution by robust electrocatalysts from secondary M (M = Cr, Fe, Co, Ni, Mo) incorporated Pt, *RSC Adv.*, **2018**, 8, 9423-9429.

26. Li, M.; Lei, Y.; Sheng, N.; Ohtsuka, T., Preparation of low-platinum-content platinum–nickel, platinum–cobalt binary alloy and platinum–nickel–cobalt ternary alloy catalysts for oxygen reduction reaction in polymer electrolyte fuel cells, *J. Power Sources*, **2015**, 294, 420-429.

27. Bi, L.; Gao, X.; Ma, Z.; Zhang, L.; Wang, D.; Xie, T., Enhanced Separation Efficiency of PtNi$_x$/g-C$_3$N$_4$ for Photocatalytic Hydrogen Production, *ChemCatChem*, **2017**, 9, 3779-3785.

28. Huang, X.Y.; Zhu, X.Y.; Zhang, X.F.; Zhang, L.; Feng, J.J.; and Wang, A.J., Simple solvothermal synthesis of uniform Pt$_{66}$Ni$_{34}$ nanoflowers as advanced electrocatalyst to significantly boost the catalytic activity and durability of hydrogen evolution reaction, *Electrochim. Acta*, **2018**, 271, 397-405.

29. Li, J.; Lu, S.; Xu, W.; He, G.; Yu, T.; Cheng, Y.; Wu, B., Fabrication of stable Ni–Al$_4$Ni$_3$–Al$_2$O$_3$ superhydrophobic surface on aluminum substrate for self-cleaning, anti-corrosive and catalytic performance, *J. Mater. Sci.*, **2018**, 53, 1097-1109.

30. Yan, H.; Zhang, D.; Xu, J.; Lu, Y.; Liu, Y.; Qiu, K.; Zhang, Y.; and Luo, Y., Solution growth of NiO nanosheets supported on Ni foam as high-performance electrodes for supercapacitors, *Nanoscale Res. Lett.*, **2014**, 9, 1-7.

31. Osman, A.I.; Abu-Dahrieh, J.K.; Rooney, D.W.; Halawy, S.A.; Mohamed, M.A.; Abdelkader, Effect of precursor on the performance of alumina for the dehydration of methanol to dimethyl ether, A., *Appl. Catal. B Environ.*, **2012**, 127, 307-315.

32. Falch, A.; Shnier, A.; Wamwangi, D.; Billing, D.; Kriek, R.J.; Geldenhuys, Z., The Effect of Sputtered Pt$_{40}$Pd$_{57}$Al$_3$ Thin Film Thickness on SO$_2$(aq) Electro-Oxidation, *Electrocatalysis*, **2019**, 10, 399-405.

33. Şennik, E.; Ürdem, S.; Erkovan, M.; Kilinç, N., Sputtered platinum thin films for resistive hydrogen sensor application, *Mater. Lett.*, **2016**, 177, 104-107.

34. Kraehnert, R.; Ortel, E.; Paul, B.; Eckhardt, B.; Kanis, M.; Liu, R.; Antoniou, A., Electrochemically dealloyed platinum with hierarchical pore structure as highly active catalytic coating, *Catal. Sci. Technol.*, **2015**, 5, 206-216.

35.   Papandrew, A.B.; Atkinson, R.W.; Goenaga, G.A.; Kocha, S.S.; Zack, J.W.; Pivovar, B.S.; Zawodzinski, T.A., Oxygen Reduction Activity of Vapor-Grown Platinum Nanotubes, *J. Electrochem. Soc.*, **2013**, 160, F848-F852.

36.   Sakaliuniene, J.; Abakevičiene, B.; Šlapikas, K.; Tamulevičius, S., Influence of magnetron sputtering deposition conditions and thermal treatment on properties of platinum thin films for positive electrode–electrolyte–negative electrode structure, *Thin Solid Films*, **2015**, 594, 101-108.

37.   Çögenli, M.S.; Mukerjee, S.; Yurtcan, A.B., Membrane Electrode Assembly with Ultra Low Platinum Loading for Cathode Electrode of PEM Fuel Cell by Using Sputter Deposition, *Fuel Cells*, **2015**, 15, 288-297.

38.   Esposito, D. V., Membraneless Electrolyzers for Low-Cost Hydrogen Production in a Renewable Energy Future, *Joule* **2017,** 1, 1-8.

39.   Gillespie, M. I.; Kriek, R. J., Hydrogen Production from a Rectangular Horizontal Filter Press Divergent Electrode-Flow-Through (DEFT™) Alkaline Electrolysis Stack, *J. Power Sources* **2017,** 372, 252-259.

40.   Gillespie, M. I.; Kriek, R. J., Scalable Hydrogen Production from a Mono-circular Filter Press Divergent Electrode-Flow-Through Alkaline Electrolysis Stack, *J. Power Sources* **2018,** 397, 204-213.

41.   Gandia, L. M.; Arzamedi, G.; Diéguez, P. M., Renewable Hydrogen Technologies: Production, Purification, Storage, Applications and Safety, Newnes: 2013.

42.   Smolinka, T.; Günther, M.; Garche, J., Stand und Entwicklungspotenzial der Wasserelektrolyse zur Herstellung von Wasserstoff aus Regenerativen Energien. Kurzfassung des Abschlussberichtes NOW-Studie, Freiburg im Breisgau **2011**.

43.   Yan, F.; Zhu, C.; Li, C.; Zhang, S.; Zhang, X.; Chen, Y., Highly Stable Three-dimensional Nickel–iron Oxyhydroxide Catalysts for Oxygen Evolution Reaction at High Current Densities, *Electrochim. Acta* **2017,** 245, 770-779.

44.   Huang, L.; Ge, X.; Dong, S., A Facile Conversion of a Ni/Fe Coordination Polymer to a Robust Electrocatalyst for the Oxygen Evolution Reaction, *RSC Adv.* **2017,** 7 (52), 32819-32825.

45.   Armstrong, R. C.; Wolfram, C.; de Jong, K. P.; Gross, R.; Lewis, N. S.; Boardman, B.; Ragauskas, A. J.; Ehrhardt-Martinez, K.; Crabtree, G.; Ramana, M. V., The Frontiers of Energy, *Nat. Energy* **2016,** 1, 15020.